High Frequency Voltage Injection Sensorless Control Technique for IPMSMs Fed by A Three-Phase Four-Switch Inverter with A Single Current Sensor

Jiadong Lu, Yihua Hu, *Senior Member, IEEE*, Xiaokang Zhang, Zheng Wang, *Senior Member, IEEE*, Jinglin Liu, *Member, IEEE*, Chun Gan, *Member, IEEE*

***Abstract*—This paper proposes a sensorless control strategy using sine-wave high-frequency (HF) voltage injection for three-phase four-switch (TPFS) inverter fed interior permanent magnet synchronous motors (IPMSMs) with a single current sensor. Three-phase currents are reconstructed by a single current sensor with modification of the inverter topology. The principle of the phase current reconstruction strategy in TPFS inverter is analyzed and the topology of the proposed drive system is illustrated. Then, the normal areas and dead zones for current reconstruction are investigated in detail, and the vector synthesis method is also explained. Furthermore, the zero vector synthesis strategy and PWM generation method are also presented, where two current sampling points are applied in each PWM cycle for phase current reconstruction. Finally, HF voltage injection-based sensorless control strategy in the proposed drive system is realized by voltage projection on the proposed *k-l* axis coordinate system. The reconstructed phase currents track the actual ones accurately, and the estimation error of the rotor position by using the reconstructed phase currents is within ±0.1 rad. The effectiveness of the proposed scheme is verified by simulation and experimental results on a 5 kW IPMSM prototype.**

***Index Terms*—Fault-tolerant control, high frequency voltage injection, interior permanent magnet synchronous motor (IPMSM), phase current reconstruction, sensorless control, three-phase four-switch inverter**

Manuscript received July 05, 2017; revised October 19, 2017 and January 11, 2018; accepted February 03, 2018. This work was supported by Shaanxi Science Technology Co-ordination and Innovation Project, China (2013KTCQ01-20, 2016KTCQ01-49). *(Corresponding author: Jinglin Liu).*

J. Lu, X. Zhang, and J. Liu are with the School of Automation, Northwestern Polytechnical University, and Shaanxi Key Laboratory of Small & Special Electrical Machine and Drive Technology, Xi'an 710129, China. (E-mail: noodle@mail.nwpu.edu.cn, dingdongdan@mail.nwpu.edu.cn, jinglinl@nwpu.edu.cn).

Y. Hu is with the Department of Electrical Engineering and Electronics, University of Liverpool, Liverpool L69 3GJ, U.K. (E-mail: y.hu35@liverpool.ac.uk).

Z. Wang is with the School of Electrical Engineering, Southeast University, Nanjing 210096, China. (E-mail: zwang@eee.hku.hk).

C. Gan is with the Department of Electrical Engineering and Computer Science, University of Tennessee, Knoxville TN 37996, USA. (E-mail: cgan@utk.edu).

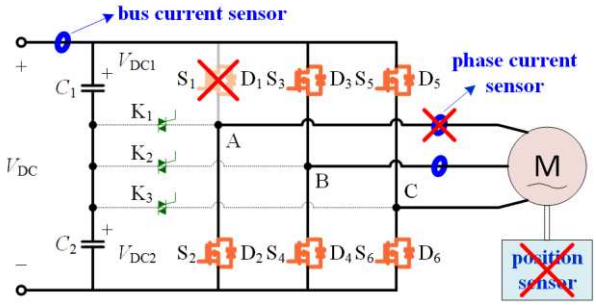

Fig. 1. Commonly occurred faults in IPMSM drive system.

I. Introduction

With the development of modern industry, the demands for reliability and cost-efficiency in the power train system increase [1]-[3]. To meet the demands, the so called fault-tolerant control technologies or money-saving solutions have been put forward. Concerning interior permanent magnet synchronous motor (IPMSM) drive system, particularly for those near the end of their operational life span periods, power switches, position sensor, and current sensor faults together with the corresponding driver or signal processing circuit faults are the commonly encountered failures as shown in Fig.1. To solve these problems, scholars proposed many solutions, such as, three-phase four-switch (TPFS) topological inverter [2]-[16], position sensorless control strategies [12], [17]-[28], and phase current reconstruction methods [29]-[39]. Over the decades, the fault-tolerant control schemes have been demonstrated to have excellent performance. However, these technologies usually focus on only one specified type of hardware fault, whereas, sometimes the drive system may simultaneously face different kinds of failures. Simple combinations of the different fault-tolerant schemes are not effective, because these methods are based on the availability of other hardware components, which are obviously broken and not available as well under this condition.

TPFS inverter is a promising topology either for the purpose of fault-tolerant control or money-saving [3]-[7]. However, it still has some innate disadvantages compared to conventional TPSS inverters. In order to take full advantage of the

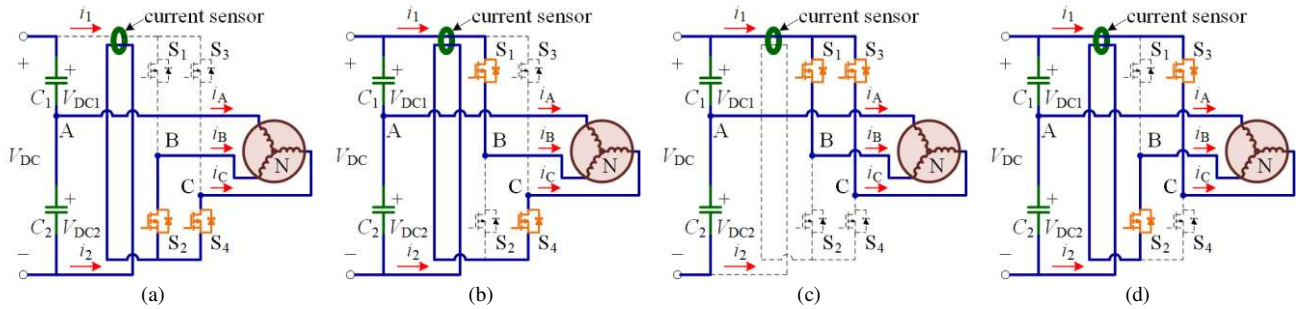

Fig. 2. The equivalent circuits of proposed IPMSM sensorless drive system fed by TPFS inverter with one single current sensor: (a) Switching state of V_{00}, (b) Switching state of V_{10}, (c) Switching state of V_{11}, (d) Switching state of V_{01}.

considerable merits of a TPFS inverter, many literatures have investigated the approaches to mitigating the negative effects of TPFS topology based circuits. Papers [4] and [7] proposed relevant control strategies to mitigate the side effects induced by the low voltage utilization factor. Some compensation measures were put forward in [3] and [11] to suppress voltage offset at the capacitor neutral point.

For the sensorless control technologies of IPMSMs, there are mainly two kinds of schemes: the model based methods for high speed applications and the salient pole tracking based methods for stand-still and low speed conditions, among which the latter is studied in this paper. High frequency (HF) signal injection is a typical strategy by using the salient pole tracking theory [18], [20]. Generally three-phase six-switch (TPSS) inverter is utilized in these schemes for signal injection and rotor position estimation [18], [20]. However, if the switches in one bridge arm of TPSS inverter are broken, as have been briefly mentioned above, these methods will become invalid due to topology change [17]. IPMSM sensorless control schemes fed by TPFS inverter was studied in [25], [26], whereas, these literatures focused on the model based methods, which are not suitable for stand-still and low speed applications. Besides, the phase currents utilized in these methods are detected by three-phase current sensors directly, which increases the system cost, hardware complexity and decreases the system reliability.

Limited by the current source output bandwidth, in most HF signal injection methods, the injected signal is HF rotating circular voltage rather than current signals. Because the rotor position is contained in HF components of the phase currents, precise detection of the phase currents is of paramount significance in the sensorless control system [23]. Usually this is implemented by installing three or at least two phase current sensors. Considering reliability and cost-efficiency, phase current reconstruction strategies have been proposed to remove the phase current sensors, and only one single bus current sensor is used. These methods are based on the relationship between the bus current and three phase currents under different switching states [29], [38]. In order to apply the phase current reconstruction technology, the vector synthesis strategy and PWM generation method need to be modified due to the existence of the current reconstruction dead zones, which is caused by power switch dead time, diode recovery time, and AD sampling time, etc. [32].

In this paper, the IPMSM sensorless control strategy fed by a TPFS inverter using a single current sensor is proposed to further increase the fault-tolerant capability of the drive system, especially when the system is near the end of its operational life span period. The proposed strategy is realized by small modification of the inverter topology and voltage projection on the proposed *k-l* axis coordinate system. The proposed strategy only needs one single current sensor and no position sensor. The principle and topology of the proposed phase current reconstruction strategy are illustrated. Afterwards, the current reconstruction dead zones and vector synthesis method are studied detailedly. Meanwhile, the zero vector synthesis scheme and PWM signals generation method are also illustrated. Finally, HF voltage injection method in the proposed drive system is deduced in detail.

This paper is organized as follows. In section II, the principle and topology of the proposed drive system are illustrated. In section III, the current reconstruction dead zones and vector synthesis method are explained. In section IV, the zero vector synthesis strategy and PWM generation method are presented. In section V, HF voltage injection method in the proposed drive system is derived. Simulation and experimental results are given in section VI and VII. The conclusion is displayed in the final section.

II. Proposed Phase Current Reconstruction Scheme in TPFS Inverter

The topology of the proposed IPMSM sensorless drive system fed by a TPFS inverter with a single current sensor is illustrated in Fig.2. In the figure, the currents flow in the defined positive directions. The current sensor is installed to detect subtraction of current i_1 and i_2, i.e., $i_1 - i_2$.

In this paper, S_b and S_c are defined to denote the switching states, where "1" represents closing state of the upper switches, whereas binary "0" represents closing state of the lower switches. Therefore, the relationships between the three-phase currents and detected current are displayed in Table I. From the table it can be seen that the three-phase currents can be calculated by using the detected current values along with any two adjacent voltage vectors. Simultaneously, any voltage vector can be synthesized by two adjacent voltage vectors, which makes it possible for phase current reconstruction in a TPFS inverter.

TABLE I
RELATIONSHIP BETWEEN THREE PHASE CURRENTS AND DETECTED CURRENT UNDER DIFFERENT SWITCHING STATES.

(S_b, S_c)	Action Vector	i_1	i_2	$i_1 - i_2$
(0, 0)	V_{00}	0	$-i_A$	$i_A = -(i_B + i_C)$
(1, 0)	V_{10}	i_B	i_C	$i_B - i_C$
(1, 1)	V_{11}	$-i_A$	0	$-i_A = i_B + i_C$
(0, 1)	V_{01}	i_C	i_B	$i_C - i_B$

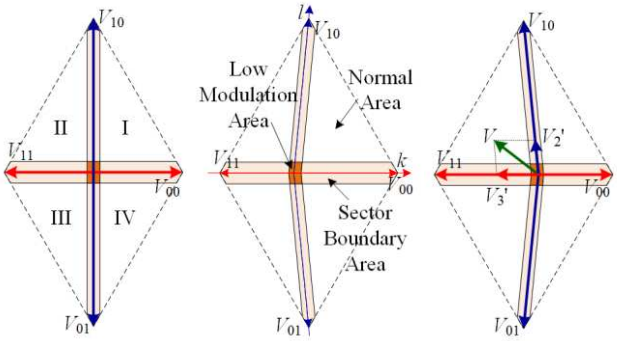

(a) (b) (c)

Fig. 3. Current reconstruction normal areas and dead zones in TPFS inverter: (a) $V_{DC1} = V_{DC2}$, (b) $V_{DC1} < V_{DC2}$, (c) $V_{DC1} > V_{DC2}$.

III. CURRENT RECONSTRUCTION DEAD ZONES AND VECTOR SYNTHESIS METHOD

As is mentioned above, due to the existence of power switch dead time, diode recovery time, and AD sampling time, the action time of any of the two vectors used in the current reconstruction scheme should reach the minimum value T_{min} during the whole switching period T_s. However, in some regions the action time of either one or both the two vectors is shorter than T_{min}, and the current reconstruction dead zones are formed in these regions, which are illustrated in Fig.3 (b). In Fig.3, the dead zones consist of two parts, i.e., the sector boundary area and low modulation area. In the normal areas, the vector synthesis method can be directly used for phase current reconstruction, whereas in the dead zones, the vector synthesis method has to be modulated before it can be used to reconstruct the phase currents.

In this paper, a vector synthesis method is proposed for current reconstruction. Any voltage vector is synthesized by the two basic adjacent voltage vectors. The situation that $V_{DC1} < V_{DC2}$ for the two unbalanced capacitor voltages is analyzed in detail.

There are four sectors in the output voltage area as shown in Fig.4 (b). Vectors V_{00} and V_{11} are in the opposite directions with different values, whereas, V_{10} and V_{01} are equal in value but in the opposite directions with angular deviation. All these factors should be considered in the vector synthesis process.

In the normal areas and current reconstruction dead zones of sector I, vectors V_{00} and V_{10} are used to synthesize the output voltage both with action time that is no shorter than T_{min}, and therefore V_{11} and V_{01} are served as the compensative voltage vectors to balance the extra voltage vector. There are similar situations in the remaining three sectors. For a better explanation, T_{00}, T_{10}, T_{11}, and T_{01} denote the action time of

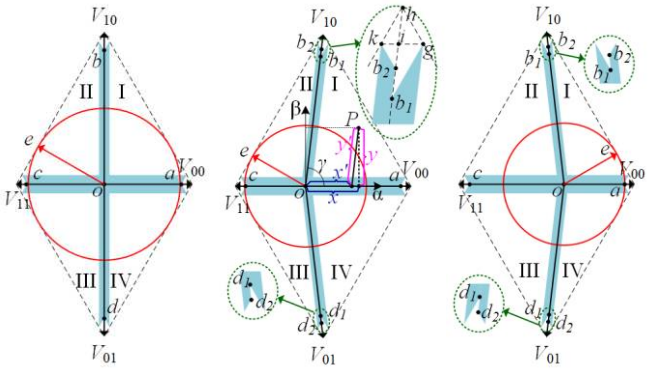

(a) (b) (c)

Fig. 4. Vector synthesis method in current reconstruction dead zones: (a) $V_{DC1} = V_{DC2}$, (b) $V_{DC1} < V_{DC2}$, (c) $V_{DC1} > V_{DC2}$.

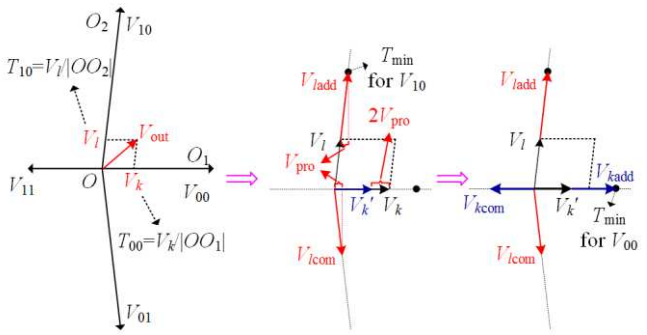

Fig. 5. Vector synthesis method in dead zones of Fig.4 (b).

vectors V_{00}, V_{10}, V_{11}, and V_{01} respectively.

To be specific, taking the vectors in section I as an example, vectors V_{00} and V_{10} are utilized to synthesize the output voltage vector. In the normal area, both T_{00} and T_{10} are longer than T_{min}, therefore, no further adjustment of T_{00} and T_{10} is required for current reconstruction. However, if the output voltage vector falls in the current reconstruction dead zones, at least one of the values of T_{00} and T_{10} is shorter than T_{min}. In this case, both the two values are additionally increased to ensure that they are not smaller than T_{min}. And vectors V_{11} and V_{01} are served as the compensation vectors. Because the additional component of V_{10} and the compensating voltage vector V_{01} have projection values on the k-axis, the action time of V_{00} for output voltage generation will be affected. In order to eliminate these additional projection values, T_{10} should be increased firstly if it is shorter than T_{min}. And then T_{00} should be compensated by taking into account the impact of the projections of the additional components of V_{10} and V_{01}. The process of calculating the action time of vectors in section I is illustrated in Fig.5, and can be summarized as

1) Calculate the action time T_{00} and T_{10} for the output voltage vector (V_{out}).
2) If T_{10} is shorter than T_{min}, it is enlarged to T_{min} (V_{ladd}), and V_{01} is utilized to compensate the extra component (V_{lcom}).
3) The projection values of the additional component of V_{10} and the compensated voltage V_{01} on the k-axis (both V_{pro}) are subtracted from T_{00} ($V_k'=V_k-2V_{pro}$).
4) T_{00} is then enlarged to T_{min} (V_{kadd}) if it is smaller than

TABLE II
THE MEANING OF POINTS IN FIG.4 (B).

Point	T_{00}	T_{10}	T_{11}
b_1	$T_{\min}$	T_s-(1+ V_{DC2}/V_{DC1}) $\cdot T_{\min}$	$T_{\min}\cdot V_{DC2}/V_{DC1}$
b_2	$T_{\min}\cdot V_{DC1}/V_{DC2}$	T_s-(1+ V_{DC1}/V_{DC2}) $\cdot T_{\min}$	$T_{\min}$
g	$T_{\min}$	T_s-$T_{\min}$	0
k	0	T_s-$T_{\min}$	$T_{\min}$

$T_{\min}$, and V_{11} is utilized to compensate the extra component ($V_{k\text{com}}$).

With the proposed voltage vector synthesis method and current reconstruction strategy, the blue areas in Fig.4 represent the available current reconstruction areas of dead zones in Fig.3. In Fig.4(b), the meanings of points 'b_1', 'b_2', 'g' , 'k' are displayed in Table II. Taking point 'b_1' for instance, in sector I, when the voltage vector falls on the l-axis, the action time of vector V_{00} is 0. However, considering the application of the current reconstruction, the action time of any of the two vectors must be longer than $T_{\min}$. Therefore, the action time of V_{00} is set to $T_{\min}$, and vector V_{11} is utilized to compensate for the surplus voltage vector component in the positive direction of V_{00}. T_{11} can be calculated as $T_{\min}\cdot V_{DC2}/V_{DC1}$. In this case, T_{10} is T_s-(1+ V_{DC2}/V_{DC1}) $\cdot T_{\min}$.

In the three figures of Fig.4, the relationships between V_{DC1} and V_{DC2} are different. Therefore, the current reconstruction dead zones on the proposed l-axis for the cases shown in Fig.4 (b) and (c) are not the same as that in Fig.4 (a), and the elliptical part with green dotted line shows an irregular shape.

$$\begin{cases} |oa| = (1-2d_{\min})V_{DC2} + d_{\min}(V_{DC2}-V_{DC1}) \\ |oc| = (1-2d_{\min})V_{DC1} - d_{\min}(V_{DC2}-V_{DC1}) \\ |ob_1| = |od_1| = (1-2d_{\min}\cdot V/V_{DC1})\cdot\sqrt{3}V/w \\ |ob_2| = |od_2| = (1-2d_{\min}\cdot V/V_{DC2})\cdot\sqrt{3}V/w \\ |oe| = \sqrt{3}V_{DC1}/2 \end{cases} \quad (1)$$

$$u = \cot\gamma = (V_{DC2}-V_{DC1})/(2\sqrt{3}V) \quad (2)$$

$$w = \sin\gamma = 1/\sqrt{1+u^2} \quad (3)$$

where, V_{DC1} and V_{DC2} are the two bus voltage values which are illustrated in Fig.2; $d_{\min}$ is the minimum duty cycle corresponding to the minimum action time $T_{\min}$; V represents the average value of the two capacitor voltages; u and w are the cotangent and sinusoidal values of γ shown in Fig.4, which denote the deviation degrees of the two DC capacitor voltages.

From Fig.4 (b), it can be seen that the judgment of actual output voltage range containing the circular output voltage is based on the following condition

$$|oc| > |oe| . \quad (4)$$

By substituting (1) into (4)

$$d_{\min} < \frac{2-\sqrt{3}}{4}\frac{V_{DC1}}{V} . \quad (5)$$

If the minimum duty cycle $d_{\min}$ dissatisfies (5), the actual circular output voltage will be reduced.

The voltage values under the three conditions in Fig.4 can be derived as

$$\begin{cases} |oa| = (1-2d_{\min})V_{DC2} + d_{\min}(V_{DC2}-V_{DC1}) \\ |oc| = (1-2d_{\min})V_{DC1} - d_{\min}(V_{DC2}-V_{DC1}) \\ |ob| = |od| = \left[1-2d_{\min}\cdot V/\min(V_{DC1},V_{DC2})\right]\cdot\sqrt{3}V/w \\ |oe| = \sqrt{3}\min(V_{DC1},V_{DC2})/2 \end{cases} . \quad (6)$$

In (6), $|ob|$ and $|od|$ represent $|ob_1|$ and $|od_1|$ respectively in both Fig.4 (b) and (c). The judgment of actual output voltage range containing the circular output voltage can be made by using the condition displayed below

$$d_{\min} < \frac{2-\sqrt{3}}{4}\frac{\min(V_{DC1},V_{DC2})}{V} . \quad (7)$$

IV. ZERO VECTOR SYNTHESIS STRATEGY AND PWM GENERATION METHOD

A. Zero vector synthesis method

A TPFS inverter inherently has no zero vector, and the equivalent zero vector can only be synthesized by the four available basic vectors. In this paper, all the four vectors V_{00}, V_{10}, V_{11}, and V_{01} are applied. By applying all the four vectors to synthesize the zero vector, the action time of all the basic vectors are increased, which is very beneficial for the accuracy improvement of phase current reconstruction. The unequal values of V_{00} and V_{11} and the incompletely opposite directions of V_{10} and V_{01} will be taken into consideration. The action time of the four vectors can be deduced as

$$\begin{cases} T_{zero\_10} = T_{zero\_01} = t/4 \\ T_{zero\_00} = t\cdot V_{DC1}/4V \\ T_{zero\_11} = t\cdot V_{DC2}/4V \\ t = \dfrac{T_{zero}}{1+\dfrac{|V_{DC1}-V_{DC2}|}{4\cdot\min(V_{DC1},V_{DC2})}} \end{cases} \quad (8)$$

where, T_{zero_00}, T_{zero_10}, T_{zero_11} and T_{zero_01} are the zero vector component time of vectors V_{00}, V_{10}, V_{11}, and V_{01}, respectively; T_{zero} is the total zero vector time.

The action time of the compensational vector used to balance the components of vectors V_{10} and V_{01} on the l-axis is

$$T_{zero\_Add} = \frac{|V_{DC1}-V_{DC2}|}{\min(V_{DC1},V_{DC2})}\cdot\frac{t}{4} \quad (9)$$

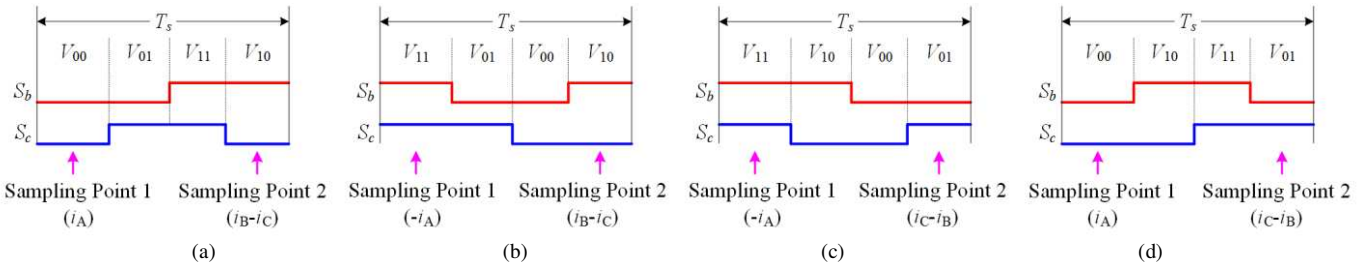

Fig. 6. PWM signals and current sampling points: (a) Sector I, (b) Sector II, (c) Sector III, (d) Sector IV.

where T_{zero_Add} is the zero vector compensation time of vectors on the *l*-axis.

If $V_{DC1}>V_{DC2}$, the compensational vector is V_{00}, otherwise the compensational vector is V_{11}.

B. PWM signals and current sampling points

In the previous part, the zero vector synthesis method is introduced. In this paper, PWM signals are derived based on the proposed zero vector synthesis method using all the four vectors. The PWM signals and current sampling points are illustrated in Fig.6. The action time of the basic vectors is calculated according to the output voltage vector and zero vector synthesis method in sections III and IV respectively. There are two bus current sampling points in each PWM cycle in the proposed phase current reconstruction scheme. The periods of the two vectors used to synthesize the output voltage vector are utilized for current reconstruction, because the action time of these two vectors are longer than that of the other two vectors. The two sampling points in each PWM cycle are in the middle of the corresponding vector action period as illustrated in Fig.6.

V. Principle of HF Voltage Injection Sensorless Control Fed by TPFS Inverter

Generally a TPSS inverter is utilized in IPMSM sensorless control schemes for signal injection and processing to estimate the rotor position. However, if the inverter is broken due to open-circuit fault of switches in one bridge arm, these methods will become invalid because of topology change. In order to apply the sensorless control technology in an IPMSM drive system fed by a TPFS inverter, some adjustments need to be made in HF voltage injection methods. The HF circular voltage signal injected into the motor winding is

$$u_h = U_h e^{i\omega_h t} \tag{10}$$

where u_h denotes the injected HF circular voltage signal; U_h represents the amplitude of the injected signal; ω_h is the electric angular velocity of the injected signal; t represents time.

In the Clark coordinate system, the injected HF signal can be described as

$$\begin{cases} u_\alpha = U_h \cos(\omega_h t) \\ u_\beta = U_h \sin(\omega_h t) \end{cases} \tag{11}$$

where u_α and u_β represent the projections of the injected HF signal on the α- and β-axis respectively in the Clark coordinate system.

In this paper, a nonorthogonal-nonlinear *k-l* axis coordinate system is utilized as shown in Fig.3 (b). In the coordinate system, V_{00} and V_{11} are in the positive and negative directions of *k*-axis respectively, whereas V_{10} and V_{01} are in the positive and negative directions of *l*-axis respectively. The corresponding representation of a $P(x, y)$ on the *k-l* axis $P(x', y')$ can be deduced as (12), which is shown in Fig.4 (b)

$$\begin{cases} x' = x - u \cdot |y| \\ y' = y / w \end{cases} \tag{12}$$

where x and y are the coordinates of point P in the Clark coordinate system; x' and y' are projections of point P on the *k-l* coordinate system.

Thus the injected HF voltage signal on the *k-l* axis can be described as

$$\begin{cases} u_k = u_\alpha - u \cdot |u_\beta| = U_h \left[\cos(\omega_h t) - u \cdot |\sin(\omega_h t)| \right] \\ u_l = u_\beta / w = U_h \sin(\omega_h t) / w \end{cases} \tag{13}$$

where u_k and u_l represent the projections of the injected HF signal in the *k-l* coordinate system.

Then the rotor position can be obtained by analyzing the HF components of the reconstructed phase currents.

VI. Simulation Results

In order to verify the effectiveness of the proposed IPMSM sensorless control strategy fed by a TPFS inverter using phase current reconstruction, simulations were carried out in MATLAB/Simulink as shown in Fig.7. The main parameters of IPMSM used in simulation are given in Table III, and the parameters of the injected HF signal are 40V, 1000Hz. The PWM switching frequency is 8 kHz, and the minimum switching state time T_{min} is set as 5 μs. In the simulation system, phase-A winding of IPMSM is connected to the neutral point of the two bus capacitors. The reconstructed three-phase currents are utilized for position estimation and speed control. For the purpose of comparison, the estimated rotor position by using the actual currents is also analyzed. In addition, different working conditions of the IPMSM are tested, including the starting mode, load disturbance mode, and speed reversing mode.

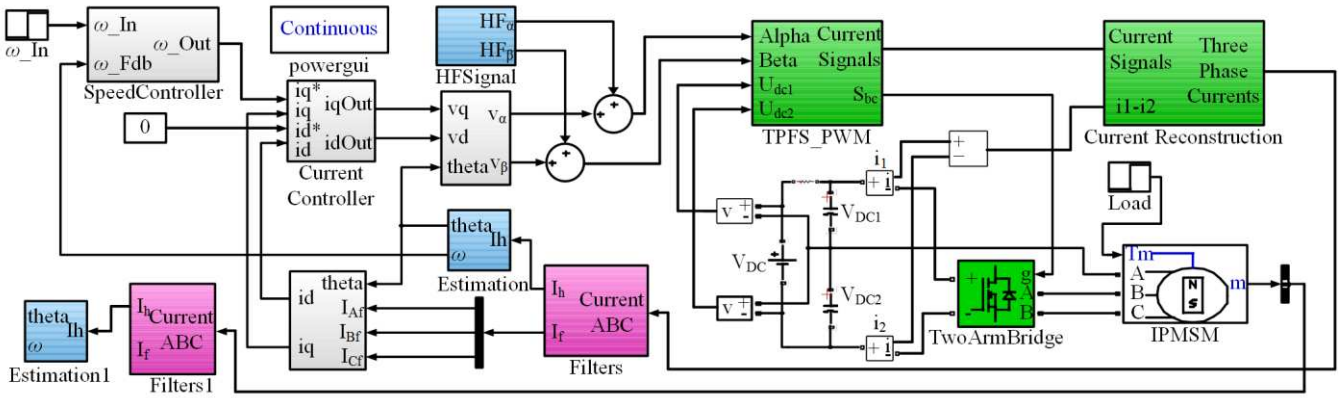

Fig. 7. Structure diagram of simulation system.

TABLE III
MAIN PARAMETERS OF IPMSM USED IN SIMULATION AND EXPERIMENT.

Parameter	Value	Parameter	Value
Rated power	5 kW	*d*-axis Inductance	4.2 mH
Inverter DC voltage	540 V	*q*-axis Inductance	10.1 mH
Rated torque	15 N·m	Phase resistance	0.18 Ω
Pole pairs	3	Maximum speed	3000 r/min
Rotor inertia	0.0023 kg·m^2		

A. *Phase current reconstruction strategy*

Fig.8 shows the simulation results of the proposed phase current reconstruction scheme. In the figure, S_b and S_c are the PWM signals of the upper switches in phase B and C. i_1-i_2 is defined as shown in Fig.2. i_A, i_B, and i_C represent the actual three-phase currents, respectively. i_A', i_B', and i_C' denote the reconstructed three-phase currents, respectively. "1st" and "2nd" denote the two sampling points for current reconstruction in each PWM cycle. The 1st sampling point in each PWM cycle is marked with the pink dotted line, and the 2nd sampling point is marked with the orange dotted line.

The output voltage vector in Fig.8 is located in sector III & IV. In sector III, the 1st sampling point lies in the action period of vector V_{11}, and the value of the detected current, $i_1 - i_2$, is $-i_A$. The 2nd sampling point lies in the action period of vector V_{01}, and the value of the detected current is $i_C - i_B$. Therefore, the reconstructed three phase currents i_A', i_B', and i_C' can be calculated after the 2nd sampling point in each PWM cycle. From Fig.8 (d), it can be seen that the proposed phase current reconstruction scheme is effective to mimic the actual three-phase currents.

B. *Sensorless control performances*

Fig.9 shows the speed response curve of the sensorless drive system. At 0.01 s the speed changes from 0 to 500 rpm with a load of 10 N·m. At 0.33 s a sudden load of 3 N·m is removed from the motor shaft. Then at 0.6 s a sudden load of 3 N·m is added to the motor shaft. Finally, at 0.83 s the output speed is set to -500 r/min (speed reverse).

In Fig.2, the phase-A winding is directly connected to the neutral point of the two bus capacitors. Therefore, the deviations of the two capacitor voltages V_{DC1} and V_{DC2} exist in

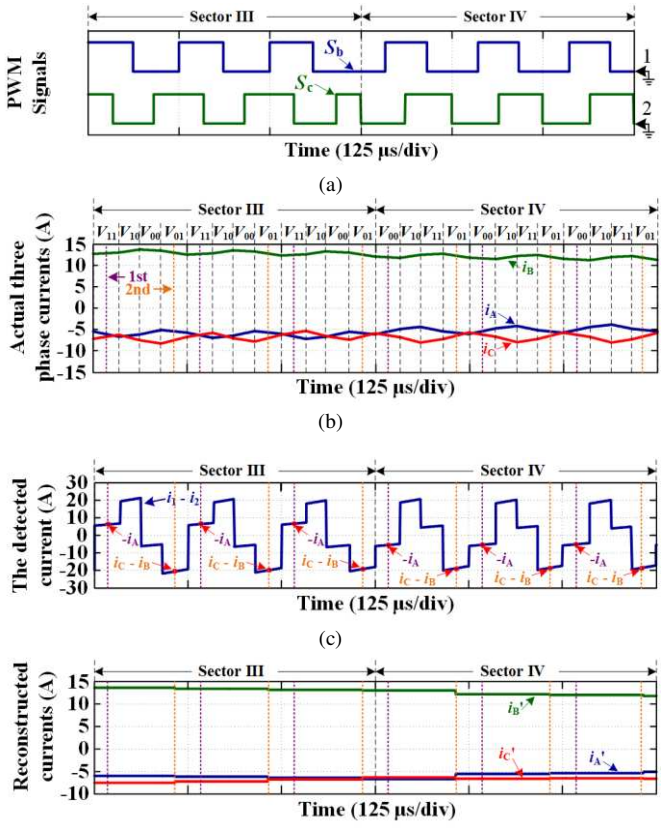

Fig. 8. Simulation results of phase current reconstruction of proposed scheme: (a) PWM signals, (b) Actual phase currents and action vector, (c) Detected current, (d) Reconstructed phase currents.

TPFS inverters. The control strategy used to eliminate the deviation of V_{DC1} and V_{DC2} in this paper is introduced in [2]. After the compensation method is utilized, the two bus capacitor voltages are displayed in Fig.10. From the figure, it can be seen that in the motor dynamic process, deviationV_{DC1} and V_{DC2} fluctuation is obvious. However, with the compensation strategy, the offset midpoint voltage can be quickly compensated.

Fig.11 shows the simulation results of the actual and reconstructed three-phase currents of the sensorless drive system. i_A, i_B, and i_C represent the actual three-phase currents, whereas i_A', i_B', and i_C' denote the reconstructed three-phase

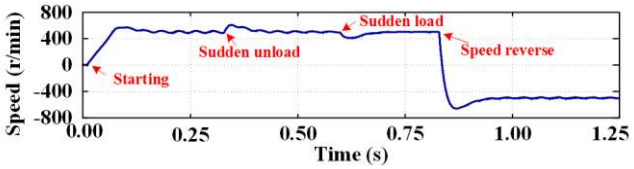

Fig. 9. Simulation results of speed response of IPMSM sensorless drive system fed by TPFS inverter.

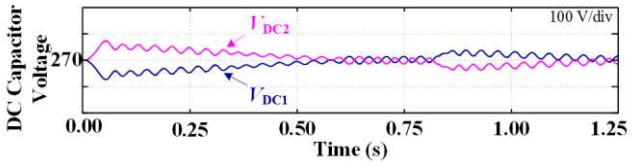

Fig. 10. Simulation results of two DC bus capacitor voltages.

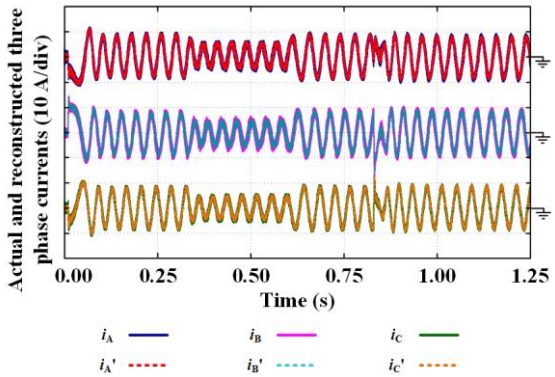

Fig. 11. Simulation results of actual and reconstructed phase currents of IPMSM sensorless drive system fed by TPFS inverter.

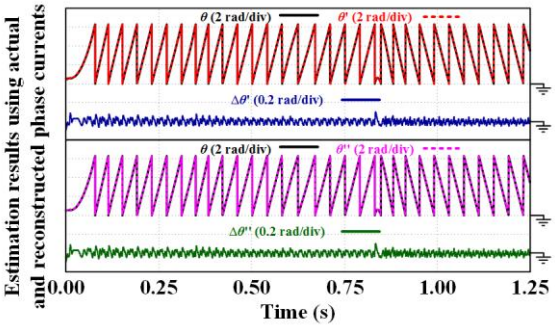

Fig. 12. Estimation results of IPMSM sensorless drive system fed by TPFS inverter using actual and reconstructed phase currents.

currents. From the figure, it can be seen that the reconstructed phase currents track the actual ones accurately, even in the dynamic process of the phase currents.

Fig.12 shows the simulation results of an IPMSM sensorless control strategy fed by a TPFS inverter: Fig.12 (a) shows the estimation results by using the actual three-phase currents, and Fig.12 (b) shows the estimation results by using the reconstructed three-phase currents. In the figure, θ denotes the actual rotor position. θ' and θ'' represent the estimated rotor positions using the actual and reconstructed three-phase currents respectively. $\Delta\theta'$ and $\Delta\theta''$ are the estimation errors corresponding to θ' and θ'' respectively. From the figure it can be clearly that seen that estimation errors of IPMSM sensorless

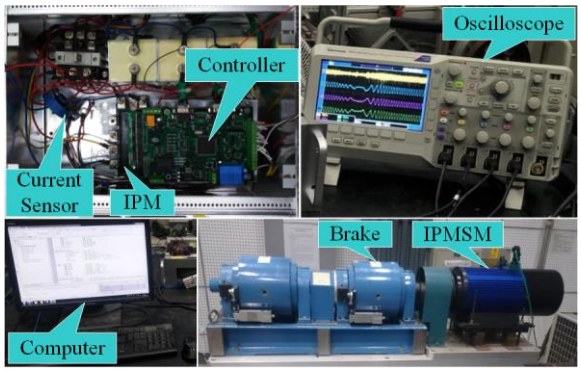

Fig. 13. Experimental setup.

drive system fed by TPFS inverter are acceptable. By applying the actual phase currents, the estimation errors are controlled within about ±0.075 rad, whereas, by applying the reconstructed phase currents, the errors are larger but are still controlled within a tolerable value of ±0.1 rad.

VII. Experimental Results

To further verify the effectiveness of the proposed IPMSM sensorless control strategy fed by TPFS inverter using a single current sensor, an experiment platform is set up as shown in Fig.13. The main parameters of IPMSM used in experiment are displayed in Table III. The parameters of the HF signal are 30V, 1000Hz. The controller is supplied by three-phase AC voltages with the amplitude of 380 V, with a rectifier and multi-level DC output power converter installed. An intelligent power module (IPM), Mitsubishi PM75RLA120, is used as PWM-VSI with the frequency of 8 kHz. Phases B and C of the motor winding are connected to the corresponding output terminals of IPM. An isolated hall-effect current sensor (HS01-100, maximum sample rate 100 kHz) is applied in the experiment platform to detect i_1-i_2 as shown in Fig.2. On the platform, a DSP, TMS320F2812, is utilized to implement the proposed strategy, sample the current, and generate PWM signals, etc.

As shown in Fig.6, two sampling points are required per control period, in which the two sampling instants are different according to the Sector and the action time of the four basic vectors. In this paper, a DSP controller is utilized to generate the PWM signals and trigger the two sampling signals. This is realized by dividing each PWM cycle (switching period, T_s=125μs) into two small ones artificially as illustrated in Fig.14 (Sector I is taken for an example). The sum of action time T_{00} and T_{01} are defined as Cycle 1, the sum of action time T_{11} and T_{10} are defined as Cycle 2. In DSP, the counter of the event manager-A (EVA) works in continuous increasing counting mode. The PWM signals are generated by the comparators of EVA with corresponding action commands in each defined small Cycle. The sampling signals are triggered by the comparison interrupt of EVA in each small Cycle. In the two Cycles, the values of the periodic register and comparison register are set with different values. In Fig.14, PR1-1 and PR1-2 are the values of the periodic register in the two Cycles, respectively. T1CMPR-1 and T1CMPR-2 are the values of the comparison register in the two Cycles, respectively. In Sector I, PR1-1 and PR1-2 are equivalent to T_{00}+T_{01} and T_{11}+T_{10},

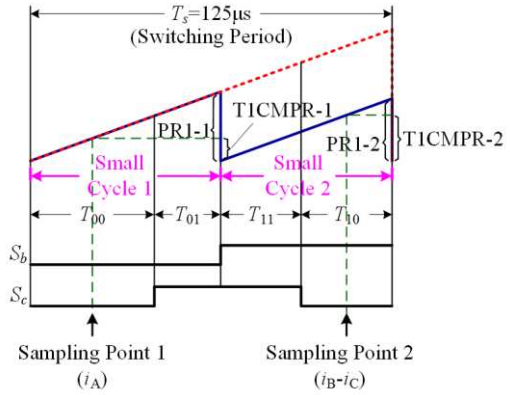

Fig. 14. PWM generation and sampling instant determination method in DSP controller, here: Sector I.

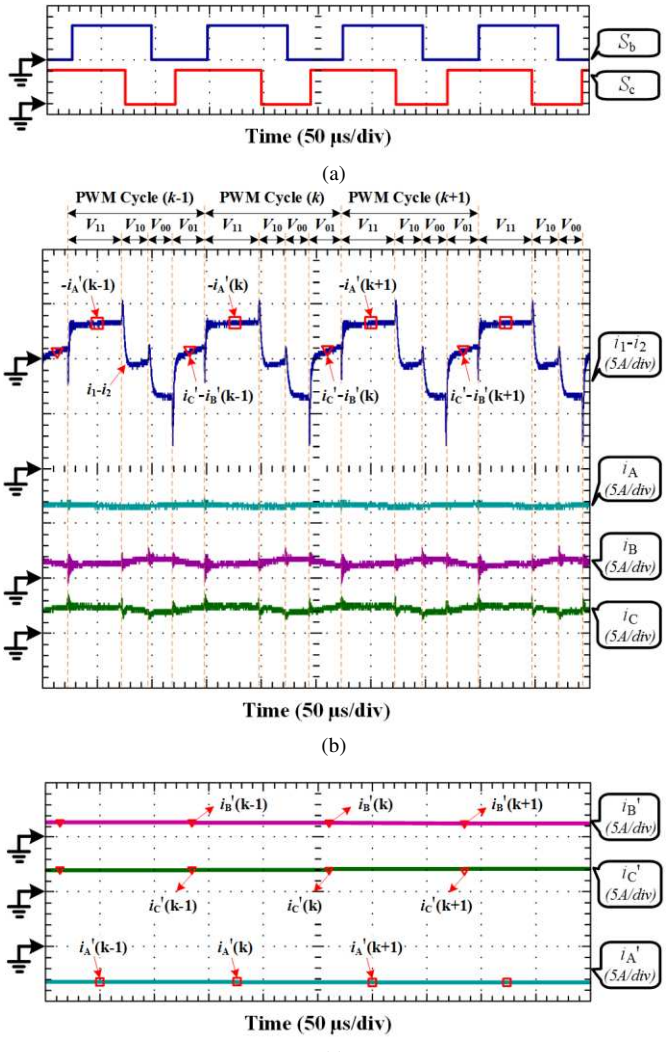

Fig. 15. Experimental results of proposed phase current reconstruction scheme (here, sector III): (a) PWM signals, (b) Detected current and actual phase currents, (c) Reconstructed phase currents.

respectively. T1CMPR-1 and T1CMPR-2 are equivalent to $T_{00}/2$ and $T_{11}+T_{10}/2$, respectively. The situations of other three Sectors are similar.

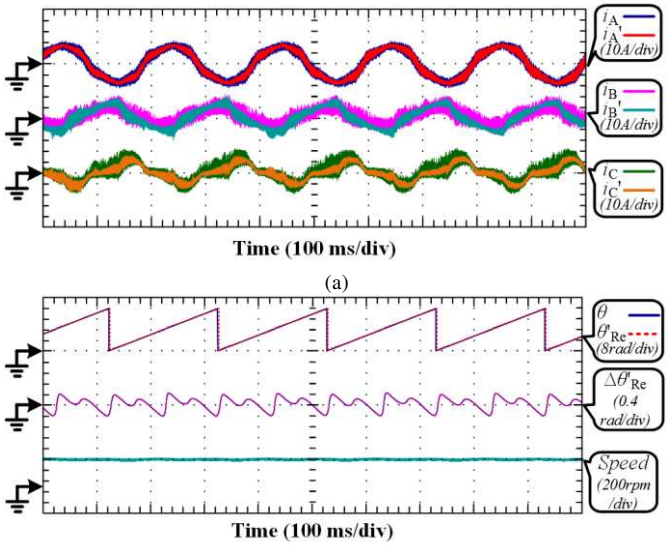

Fig. 16. Experimental results of proposed scheme in constant speed mode (speed=100 rpm): (a) Actual and reconstructed phase currents, (b) Estimation results and output speed.

A. *Phase current reconstruction strategy*

The experimental results of the proposed phase current reconstruction scheme are displayed in Fig.15 (here, sector III). In the figure, S_b and S_c are respectively the PWM signals of the upper switches in phase B and C. i_1-i_2 is defined as shown in Fig.2. i_A, i_B, and i_C represent the actual three-phase currents respectively. i_A', i_B', and i_C' denote the reconstructed three-phase currents respectively. Labels (k-1), (k), and (k+1) represent the PWM cycle sequences. The period of each PWM cycle is 125 μs, in which the two sampling points are in the middle of the corresponding vector periods and are marked with different symbols.

In sector III, the sequences of the action vectors are V_{11}, V_{10}, V_{00} and V_{01} in each PWM cycle. Therefore, in the figure, the waveform of current i_1-i_2 has four stages corresponding to the sequences of the four vectors: -i_A', i_B'-i_C', i_A' and i_C'-i_B'. The first sampling point in each PWM cycle is for current -i_A' with square symbols; the second sampling point in each PWM cycle is for i_C'-i_B' with inverted triangle symbols. From the figure it can be seen that the reconstructed three-phase currents track the actual ones accurately.

B. *Sensorless control performances*

Fig.16 shows the experimental results of the proposed IPMSM sensorless control strategy fed by a TPFS inverter using one single current sensor in the constant speed mode. Fig.16 (a) shows the actual and reconstructed three-phase currents. Fig.16 (b) presents the rotor position estimation results and the actual output speed of the drive system. The motor speed is set to 100 rpm in this condition. Compared to the waveform in simulation, the experimental results of actual currents have more burrs. This is due to the presence of white noise in the system and interference of the current sensor. In addition, the existence of HF current components also causes non-sinusoidal waveforms. However, the performance of the

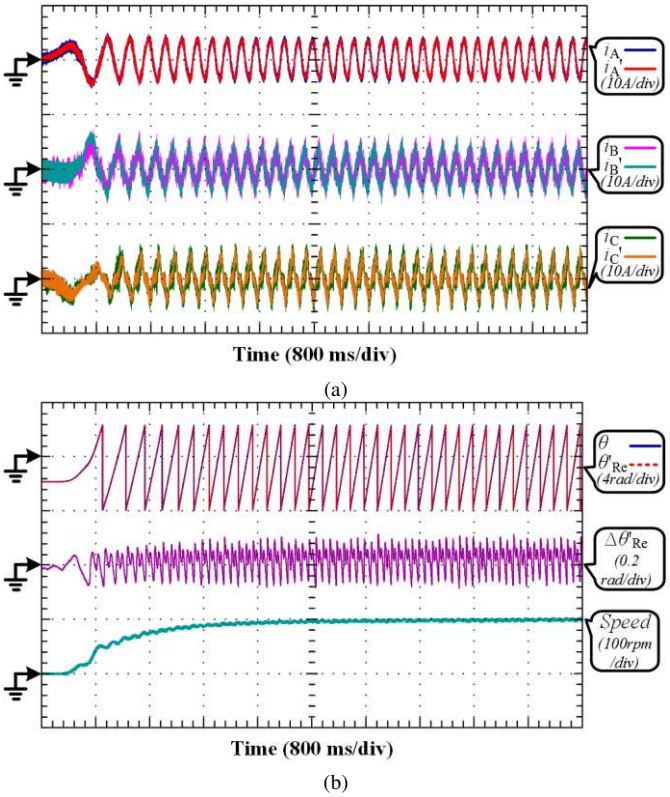

Fig. 17. Experimental results of proposed scheme in starting mode (speed from 0 rpm to 100 rpm): (a) Actual and reconstructed phase currents, (b) Estimation results and output speed.

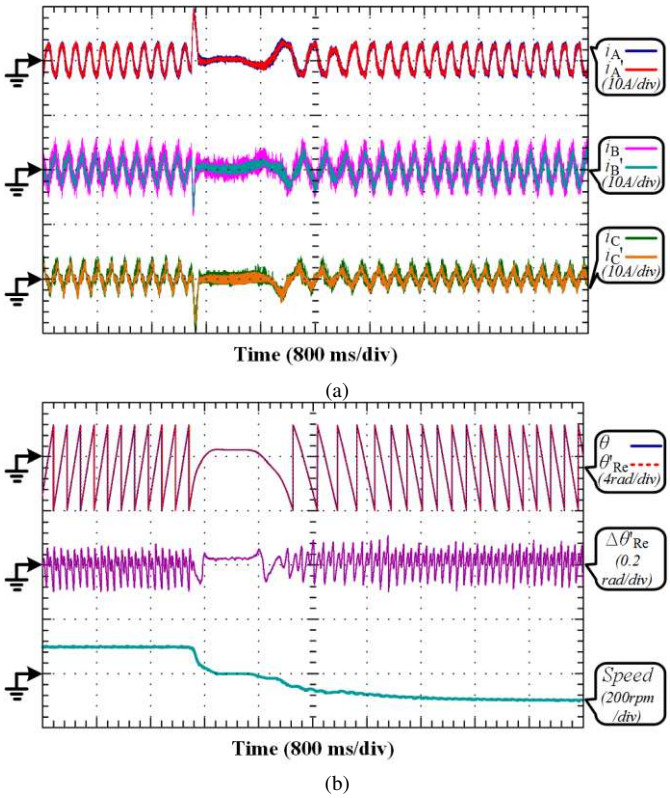

Fig. 18. Experimental results of proposed scheme in speed reversing mode (speed changes from 100 rpm to -100 rpm): (a) Actual and reconstructed phase currents, (b) Estimation results and output speed.

drive system is acceptable, since the estimated rotor position tracks the actual one accurately. The estimation error is controlled within ±0.1 rad. The output speed is stable at 100 rpm.

To further prove the applicability of the proposed strategy, the experimental results in the starting mode are displayed in Fig.17. Fig.17 (a) illustrates the current reconstruction results. Fig.17 (b) shows the actual and estimated rotor positions together with the output speed of IPMSM. In the experiment process, the motor speed command changes from 0 rpm to 100 rpm. In this case, the reconstructed three-phase currents track the actual ones well. In the figure, the estimation error is controlled within ±0.1 rad. The motor speed rises steadily from 0 to 100 rpm.

In order to validate the effectiveness of the proposed strategy in fast dynamic process of the system, experiments have been carried out in the speed reversing mode of the motor. The speed command changes to -100 rpm abruptly when the motor is running at 100 rpm steadily. The experimental results in this condition are illustrated in Fig.18. Fig.18 (a) exhibits the experimental results of the actual and reconstructed three-phase currents. Fig.18 (b) shows the experimental results of position estimation and output motor speed. In the figure, the actual currents change fast in the speed reversing process. It can be seen that in the fast dynamic process the reconstructed three-phase currents can also track the actual ones well. The estimation error is controlled within ±0.1 rad. The output motor speed follows the command smoothly from 100 rpm to -100 rpm.

VIII. Conclusion

An IPMSM sensorless control system fed by a TPFS inverter using a single current sensor is proposed in this paper. To implement the proposed strategy, three-phase currents are reconstructed from the bus current by the single current sensor with topology change. The principle of the proposed phase current reconstruction strategy is studied in detail. The zero vector synthesis method is deduced and the corresponding PWM generation method together with current sampling points in each PWM cycle is illustrated. The sensorless control strategy using HF voltage injection in the proposed drive system is investigated. The effectiveness of the proposed IPMSM sensorless control scheme using a single current sensor is verified by the simulation and experimental results on a 5 kW IPMSM prototype.

The main contributions of this paper are listed as follows.

1) A low-cost IPMSM drive is proposed by using one current sensor without position sensors. The proposed TPFS inverter only needs a small modification of the inverter topology based on the conventional one, which achieves the fault-tolerant ability when one bridge arm of the inverter fails.
2) The two current sampling points for current reconstruction are within the period of action vectors in each PWM cycle. Therefore, no additional voltage pulses is required for current reconstruction.
3) A *k-l* axis coordinate system is proposed for sector

identification and vector projection, which is simple and effective for the proposed strategy.

From the results, it can be seen that the reconstructed phase currents track the actual ones accurately in different working conditions, e.g., the constant speed mode, starting mode and speed reversing mode. The estimation error of the drive system by using the reconstructed phase currents is within ±0.1 rad, which is promising. By using the proposed scheme, the cost of IPMSM drive system can be significantly reduced and the reliability can be improved accordingly.

REFERENCES

[1] Z. Wang, Y. B. Wang, J. Chen, and M. Cheng, " Fault tolerant control of NPC three-level inverters fed double-stator-winding PMSM drives based on vector space decomposition," *IEEE Trans. Ind. Electron.,* DOI: 10.1109/TIE.2017.2701782, 2017.

[2] Z. Y. Zeng, W. Y. Zheng, R. X. Zhao, C. Zhu, and Q. W. Yuan, "Modeling, modulation and control of the three-phase four-switch PWM rectifier under balanced voltage," *IEEE Trans. Power Electron.*, vol. 31, no. 7, pp. 4892-4906, July, 2016.

[3] D. H. Zhou, J. Zhao, and Y. Liu, "Predictive Torque Control Scheme for Three-Phase Four-Switch Inverter-Fed Induction Motor Drives With DC-Link Voltages Offset Suppression," *IEEE Trans. Power Electron.,* vol. 30, no. 6, pp. 3309-3318, June, 2015.

[4] M. S. Diab, A. Elserougi, A. M. Massoud, A. S. A. Khalik, and S. Ahmed, "A Four-Switch Three-Phase SEPIC-Based Inverter," *IEEE Trans. Power Electron.,* vol. 30, no. 9, pp. 4891-4905, Sep., 2015.

[5] N. M. A. Freire and A. J. M. Cardoso, "A Fault-Tolerant PMSG Drive for Wind Turbine Applications With Minimal Increase of the Hardware Requirements," *IEEE Trans. Ind. Appl.,* vol. 50, no. 3, pp. 2039-2049, May/June, 2014.

[6] N. M. A. Freire and A. J. M. Cardoso, "A Fault-Tolerant Direct Controlled PMSG Drive for Wind Energy Conversion Systems," *IEEE Trans. Ind. Electron.,* vol. 61, no. 2, pp. 821-834, Feb., 2014.

[7] C. L. Xia, Y. W. Xiao, T. N. Shi, and W. Chen, "Boost Three-Effective-Vector Current Control Scheme for a Brushless DC Motor With Novel Five-Switch Three-Phase Topology," *IEEE Trans. Power Electron.,* vol. 29, no. 12, pp. 6581-6592, Dec., 2014.

[8] B. E. Badsi, B. Bouzidi, and A. Masmoudi, "DTC Scheme for a Four-Switch Inverter-Fed Induction Motor Emulating the Six-Switch Inverter Operation," *IEEE Trans. Power Electron.,* vol. 28, no. 7, pp. 3528-3538, July, 2013.

[9] S. Dasgupta, S. N. Mohan, S. K. Sahoo, and S. K. Panda, "Application of Four-Switch-Based Three-Phase Grid-Connected Inverter to Connect Renewable Energy Source to a Generalized Unbalanced Microgrid System," *IEEE Trans. Ind. Electron.,* vol. 60, no. 3, pp. 1204-1215, Mar., 2013.

[10] R. Wang, J. Zhao, and Y. Liu, "A Comprehensive Investigation of Four-Switch Three-Phase Voltage Source Inverter Based on Double Fourier Integral Analysis," *IEEE Trans. Power Electron.,* vol. 26, no. 10, pp. 2774-2787, Oct., 2011.

[11] K. D. Hoang, Z. Q. Zhu, and M. P. Foster, "Influence and Compensation of Inverter Voltage Drop in Direct Torque-Controlled Four-Switch Three-Phase PM Brushless AC Drives," *IEEE Trans. Power Electron.,* vol. 26, no. 8, pp. 2343-2357, Aug., 2011.

[12] C. L. Xia, Z. Q. Li, and T. N. Shi, "A Control Strategy for Four-Switch Three-Phase Brushless DC Motor Using Single Current Sensor," *IEEE Trans. Ind. Electron.,* vol. 56, no. 6, pp. 2058-2066, June, 2009.

[13] M. N. Uddin, T. S. Radwan, and M. A. Rahman, "Fuzzy-logic-controller-based cost-effective four-switch three-phase inverter-fed IPM synchronous motor drive system," *IEEE Trans. Ind. Appl.,* vol. 42, no. 1, pp. 21-30, Jan./Feb., 2006.

[14] M. B. D. R. Corrêa, C. B. Jacobina, E. R. C. D. Silva, and A. M. N. Lima, "A General PWM Strategy for Four-Switch Three-Phase Inverters," *IEEE Trans. Power Electron.,* vol. 21, no. 6, pp. 1618-1627, Nov., 2006.

[15] B. K. Lee, T. H. Tim, and M. Ehsani, "On the feasibility of four-switch three-phase BLDC motor drives for low cost commercial applications: topology and control," *IEEE Trans. Power Electron.,* vol. 18, no. 1, pp. 164-172, Jan., 2003.

[16] F. Blaabjerg, D. A. Neacsu, and John K. Pedersen, "Adaptive SVM to Compensate DC-Link Voltage Ripple for Four-Switch Three-Phase Voltage-Source Inverters," *IEEE Trans. Power Electron.,* vol. 14, no. 4, pp. 743-752, July, 1999.

[17] A. Gaeta, G. Scelba, and A. Consoli, "Sensorless Vector Control of PM Synchronous Motors During Single-Phase Open-Circuit Faulted Conditions," *IEEE Trans. Ind. Appl.,* vol. 48, no. 6, pp. 1968-1979, Nov./Dec., 2012.

[18] S. Medjmadj, D. Diallo, M. Mostefai, C. Delpha, and A. Arias, "PMSM Drive Position Estimation: Contribution to the High-Frequency Injection Voltage Selection Issue," *IEEE Trans. Energy Convers.,* vol. 30, no. 1, pp. 349-358, Mar., 2015.

[19] B. Akin, U. Orguner, A. Ersak, and M. Ehsani, "Simple Derivative-Free Nonlinear State Observer for Sensorless AC Drives," *IEEE/ASME Trans. Mechatronics,* vol. 11, no. 5, pp. 634-643, Oct., 2006.

[20] P. L. Xu and Z. Q. Zhu, "Novel Square-Wave Signal Injection Method Using Zero-Sequence Voltage for Sensorless Control of PMSM Drives," *IEEE Trans. Ind. Electron.,* vol. 63, no. 12, pp. 7444-7454, Dec., 2016.

[21] S. B. Ozturk and H. A. Toliyat, "Direct Torque and Indirect Flux Control of Brushless DC Motor," *IEEE/ASME Trans. Mechatronics,* vol. 16, no. 2, pp. 351-360, Mar., 2010.

[22] T. D. Nguyen, G. Foo, K. J. Tseng and D. M. Vilathgamuwa, "Modeling and Sensorless Direct Torque and Flux Control of a Dual-Airgap Axial Flux Permanent-Magnet Machine With Field-Weakening Operation," *IEEE/ASME Trans. Mechatronics,* vol. 19, no. 2, pp. 412-422, Apr., 2014.

[23] G. L. Wang, L. Yang, G. Q. Zhang, X. G. Zhang, and D. G. Xu, "Comparative Investigation of Pseudorandom High-Frequency Signal Injection Schemes for Sensorless IPMSM Drives," *IEEE Trans. Power Electron.,* vol. 32, no. 3, pp. 2123-2132, Mar., 2017.

[24] X. D. Sun, L. Chen, Z. B. Yang and H. Q. Zhu, "Speed-Sensorless Vector Control of a Bearingless Induction Motor With Artificial Neural Network Inverse Speed Observer," *IEEE/ASME Trans. Mechatronics,* vol. 18, no. 4, pp. 1357-1366, Aug., 2013.

[25] A. H. Niasar, A. Vahedi, and H. Moghbelli, "A Novel Position Sensorless Control of a Four-Switch, Brushless DC Motor Drive Without Phase Shifter," *IEEE Trans. Power Electron.,* vol. 23, no. 6, pp. 3079-3087, Nov., 2008.

[26] C. T. Lin, C. W. Hung, and C. W. Liu, "Position Sensorless Control for Four-Switch Three-Phase Brushless DC Motor Drives," *IEEE Trans. Power Electron.,* vol. 23, no. 1, pp. 438-444, Jan., 2008.

[27] Y. Y. Li and G. T. C. Chiu, "Control of loudspeakers using disturbance-observer-type velocity estimation," *IEEE/ASME Trans. Mechatronics,* vol. 10, no. 1, pp. 111-117, Feb., 2005.

[28] Z. Wang, Y. Zheng, Z. X. Zou, and M. Cheng, "Position sensorless control of interleaved CSI fed PMSM drive with extended Kalman filter," *IEEE Trans. Magn.,* vol. 48, no. 11, pp. 3688-3691, Nov. 2012.

[29] Y. X. Xu, H. Yan, J. B. Zou, B. C. Wang, and Y. H. Li, "Zero Voltage Vector Sampling Method for PMSM Three-Phase Current Reconstruction Using Single Current Sensor," *IEEE Trans. Power Electron.,* vol. 32, no. 5, pp. 3797-3807, May, 2017.

[30] H. F. Lu, X. M. Cheng, W. L. Qu, S. Sheng, Y. T. Li, and Z. Y. Wang, "A Three-Phase Current Reconstruction Technique Using Single DC Current Sensor Based on TSPWM," *IEEE Trans. Power Electron.,* vol. 29, no. 3, pp. 1542-1550, Mar., 2014.

[31] B. Hafez, A. S. A. Khalik, A. M. Massoud, S. Ahmed, and R. D. Lorenz, "Single-Sensor-Based Three-Phase Permanent-Magnet Synchronous Motor Drive System With Luenberger Observers for Motor Line Current Reconstruction," *IEEE Trans. Ind. Appl.,* vol. 50, no. 4, pp. 2602-2613, July/Aug., 2014.

[32] Y. S. Lai, Y. K. Lin, and C. W. Chen, "New Hybrid Pulsewidth Modulation Technique to Reduce Current Distortion and Extend Current Reconstruction Range for a Three-Phase Inverter Using Only DC-link Sensor," *IEEE Trans. Power Electron.,* vol. 28, no. 3, pp. 1331-1337, Mar., 2013.

[33] Y. Cho, T. LaBella, and J. S. Lai, "A Three-Phase Current Reconstruction Strategy With Online Current Offset Compensation Using a Single Current Sensor," *IEEE Trans. Ind. Electron.,* vol. 59, no. 7, pp. 2924-2933, July, 2012.

[34] Y. K. Gu, F. L. Ni, D. P. Yang, and H. Liu, "Switching-State Phase Shift Method for Three-Phase-Current Reconstruction With a Single DC-Link Current Sensor," *IEEE Trans. Ind. Electron.,* vol. 58, no. 11, pp. 5186-5194, Nov., 2011.

[35] K. Sun, Q. Wei, L. P. Huang, and K. Matsuse, "An Overmodulation Method for PWM-Inverter-Fed IPMSM Drive With Single Current

Sensor," *IEEE Trans. Ind. Electron.,* vol. 57, no. 10, pp. 3395-3404, Oct., 2010.
[36] J. I. Ha, "Voltage Injection Method for Three-Phase Current Reconstruction in PWM Inverters Using a Single Sensor," *IEEE Trans. Power Electron.,* vol. 24, no. 3, pp. 767-775, Mar., 2009.
[37] D. P. Marčetić and E. M. Adžić, "Improved Three-Phase Current Reconstruction for Induction Motor Drives With DC-Link Shunt," *IEEE Trans. Ind. Electron.,* vol. 57, no. 7, pp. 2454-2462, July, 2010.
[38] H. Kim and T. M. Jahns, "Phase Current Reconstruction for AC Motor Drives Using a DC Link Single Current Sensor and Measurement Voltage Vectors," *IEEE Trans. Power Electron.,* vol. 21, no. 5, pp. 1413-1419, Sep., 2006.
[39] W. C. Lee, D. S. Hyun, and T. K. Lee, "A Novel Control Method for Three-Phase PWM Rectifiers Using a Single Current Sensor," *IEEE Trans. Power Electron.,* vol. 15, no. 5, pp. 861-870, Sep., 2000.

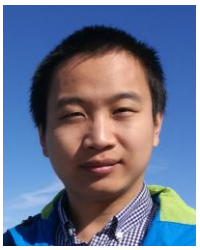

Jiadong Lu was born in Pucheng, China, 1990. He received the B.S. and the M.S. degrees in electrical engineering from Northwestern Polytechnical University, Xi'an, China in 2012 and 2015, respectively, where he is currently working toward the Ph.D. degree. In 2017, he was with the Department of Electrical Engineering and Electronics, University of Liverpool (UoL) as a research assistant.

His research interests include sensorless control and hybrid fault tolerant control techniques for permanent magnet synchronous motor drives.

Yihua Hu (M'13-SM'15) received the B.S. degree in electrical motor drives in 2003, and the Ph.D. degree in power electronics and drives in 2011, both from China University of Mining and Technology, Jiangsu, China. Between 2011 and 2013, he was with the College of Electrical Engineering, Zhejiang University as a Postdoctoral Fellow. Between November 2012 and February 2013, he was an academic visiting scholar with the School of Electrical and Electronic Engineering, Newcastle University, Newcastle upon Tyne, UK. Between 2013 and 2015, he worked as a Research Associate at the power electronics and motor drive group, the University of Strathclyde. Currently, he is a Lecturer at the Department of Electrical Engineering and Electronics, University of Liverpool (UoL). He has published more than 50 peer reviewed technical papers in leading journals. His research interests include PV generation system, power electronics converters & control, and electrical motor drives.

Xiaokang Zhang was born in Zhejiang, China, in 1992. He received the B.S degree in electrical engineering from Northeast Agricultural University, Harbin, China, in 2015 and he is currently working toward the M.S degree in electrical engineering in Northwestern Polytechnical University.

His research interests include sensorless control for permanent magnet synchronous motor and fault tolerant control techniques for motor drives.

Zheng Wang (S'05–M'09-SM'14) received the B.Eng. and M.Eng. degrees from Southeast University, Nanjing, China, in 2000 and 2003, respectively, and the Ph.D. degree from The University of Hong Kong, Hong Kong, in 2008, all in electrical engineering.

From 2008 to 2009, he was a Postdoctoral Fellow in Ryerson University, Toronto, ON, Canada. He is currently a full Professor in the School of Electrical Engineering, Southeast University, China. His research interests include electric drives, power electronics, and distributed generation. He has authored or coauthored over 80 internationally refereed papers and four books in these areas.

Prof. Wang received several academic awards including IEEE PES Chapter Outstanding Engineer Award, Best Paper Award of International Conference on Electrical Machines and Systems (ICMES), Best Session Paper Award of IEEE Annual Meeting of Industrial Electronics (IECON), and Nanjing Outstanding Paper Award of Natural Science.

Jinglin Liu (M'01) received the B.Eng. degree in electrical engineering from Tsinghua University, Beijing, China, in 1986, and the M.Eng. and the Ph.D. degrees in electrical engineering from Northwestern Polytechnical University, Xi'an, China, in 1990 and 2002, respectively. Since 1994, he has been a Faculty Member with Northwestern Polytechnical University, Xi'an, where he is currently a Professor of Electrical Engineering.

His research interests include electrical machines design and drives, power electronics, fault diagnosis, and motion control.

Chun Gan (S'14–M'16) received the B.S. and M.S. degrees in power electronics and motor drives from China University of Mining and Technology, Jiangsu, China, in 2009 and 2012, respectively, and the Ph.D. degree in power electronics and motor drives from Zhejiang University, Hangzhou, China, in 2016.

He is currently a Research Associate with the Department of Electrical Engineering and Computer Science, The University of Tennessee, Knoxville, TN, USA. He is also a member of the U.S. Energy/National Science Foundation cofunded Engineering Research Center CURENT. He has published more than 40 technical papers in leading journals and conference proceedings, and authored one book chapter. He has ten issued/published invention patents. His research interests include high-efficiency power converters, electric vehicles, electrical motor drives, electrical motor design, continuous variable series reactors, high-voltage direct current transmission, and microgrids.

Dr. Gan received the 2015 Top Ten Excellent Scholar Award, the 2016 Excellent Ph.D. Graduate Award, the 2015 Ph.D. National Scholarship, the 2015 Wang Guosong Scholarship, and the 2014 and 2015 Outstanding Ph.D. Candidate Awards in Zhejiang University.